ACS OMEGA

Open Access

http://pubs.acs.org/journal/acsodf

Article

Enhanced n-Type Thermoelectric Properties and Structure Evolution of Carbonized Metal-Coordination Polydopamine

Qi Zhu, Zhijun Wang,* Hongwen Cao, Ziheng Xu, Rui Zhong, Yihan Wang,* Bo Jiang, Qinjian Yin, and Kun Zhang

Cite This: *ACS Omega* 2024, 9, 25812−25821

Read Online

ACCESS | Metrics & More | Article Recommendations | Supporting Information

ABSTRACT: Carbonized polydopamine (cPDA) exhibits a nitrogenous graphite-like structure with n-type semiconductor property. However, the low electrical conductivity and Seebeck coefficient of cPDA cannot meet the needs of flexible thermoelectric devices. In this study, a series of metal ions were coordinated with cPDA to enhance n-type thermoelectric properties. At 300 K, all metal-coordination cPDA (metal-cPDA) samples obtain lower thermal conductivity compared to cPDA. Mn-cPDA exhibits the greatest Seebeck coefficient of −25.94 μV K^{-1}, which is almost six times higher than cPDA. Fe-cPDA shows the best electrical conductivity of 2.45 × 10^5 S m^{-1}. An optimal power factor (PF) value of 11.93 μW m^{-1} K^{-2} is achieved in Ca-cPDA with the enhanced electrical conductivity of 9.5 × 10^4 S m^{-1} and Seebeck coefficient of −11.24 μV K^{-1}. Using Fourier transform infrared spectroscopy (FTIR), energy dispersive X-ray spectroscopy (EDX), X-ray photoelectron spectroscopy (XPS), Raman spectroscopy, X-ray diffraction (XRD), and transmission electron microscopy (TEM), we revealed the structural characterization of metal-cPDA. Our results indictate that the different metal ions (Mn^{2+}, Zn^{2+}, Mg^{2+}, Al^{3+}, Ca^{2+}, and Fe^{3+}) exert varying influences on the growth of graphite-like structure within metal-cPDA, which lead to the evolution of electrical conductivity. We observe that the carrier density and carrier mobility depend on both the degree of graphitization and the metal-ion coordination, which work together on electrical conductivity and Seebeck coefficient. These findings and understanding of the thermoelectric properties of PDA-based materials will help to realize high-performance n-type thermoelectric materials for flexible electronic device applications.

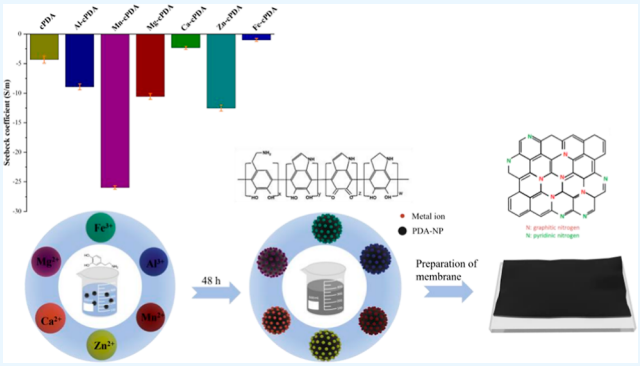

1. INTRODUCTION

Thermoelectric materials have the capacity to transform waste thermal energy into valuable electrical power, and the efficiency of this conversion is measured by the dimensionless figure of merit ZT = $S^2\sigma T/\kappa$, where S is the Seebeck coefficient, σ is the electrical conductivity, κ is the thermal conductivity, and T is the absolute temperature. Thermoelectric generators necessitate the incorporation of both p-type (hole-transporting) and n-type (electron-transporting) conducting materials.[1−3] Currently, p-type materials have garnered considerable attention and have seen substantial advancements, whereas n-type materials still lag in development.[4] Unlike inorganic thermoelectric materials, organic thermoelectric materials are characterized by lightweight, high flexibility, and low intrinsic thermal conductivity, which offer unique benefits for applications such as flexible electronics, power generation, and cooling at low or microscale temperature gradients.[5−7]

Recently, there has been an emergence of the polymer-based materials exhibiting n-type properties. Polydopamine (PDA), the synthetic analog of natural melanin, is widely used as a multifunctional surface coating material and a novel type of carbon nanoparticle.[8−12] Owing to the superior adhesion of PDA, it has also been employed to cross-link conducting polymers and carbon materials with excellent conductivities, thereby enhancing thermoelectric performance.[13] Under weakly alkaline conditions (pH ∼ 8.5), PDA is generated by the self-polymerization of the dopamine (DA) monomer. PDA can be carbonized by pyrolysis annealing (600−900 °C) in an inert atmosphere, and carboned PDA (cPDA) exhibits a short-range ordered and nitrogen-containing graphitic structure with superior electrical conductivity.[14] The fabrication procedure of cPDA is both environmentally benign and straightforward, positioning it as a promising candidate for nanostructured carbon materials. The fascinating feature of cPDA is its n-type

Received: January 3, 2024
Revised: April 25, 2024
Accepted: April 26, 2024
Published: June 7, 2024

semiconductor behavior due to the presence of nitrogen heteroatoms in the carbon skeleton,[9,11] which enables the creation of novel n-type thermoelectric materials.

One category of materials that shows promise for thermoelectric applications consists of π-conjugated transition-metal coordination polymers. These materials exhibit high electrical conductivity and an n-type Seebeck coefficient, a result of the interaction between the delocalized π orbitals of the organic polymer and the localized d orbitals of the transition metal.[15] Sun et al. reported that the poly(Ni-ethylenetetrathiolate) powder showed a ZT value of 0.2 with a Seebeck coefficient of -150 μV K^{-1} and a conductivity of 60 S cm^{-1} at 400 K in 2012,[16] and achieved the highest ZT value of 0.3 at 400 K for n-type thermoelectrical materials in 2016.[17] Nevertheless, these materials suffer from low stability in the air, which limits their potential applications.

Motivated by the high affinity of PDA to a broad spectrum of metal ions, attributable to the functional groups such as catechol, amine, and imine, it is anticipated that the metal-coordinated PDA-based materials, after high-temperature annealing, would exhibit enhanced n-type thermoelectric properties. However, Li et al. introduced Na^+, Mg^{2+}, and Cu^{2+} into cPDA, but the metal-containing cPDA (metal-cPDA) materials did not show significant improvement in electrical conductivity or Seebeck coefficient.[18] Moreover, most of the research on metal-polydopamine (metal-PDA) and its derived materials focus on enhancing their electrical, thermal, and mechanical properties, but their thermoelectric properties have received less attention. In this study, we report the enhanced Seebeck coefficient and electrical conductivity of metal-cPDA, achieved by incorporating a metal salt during the synthesis of PDA. The interplay between the structural characteristics and the thermoelectric properties of the materials was elucidated by Fourier transform infrared spectroscopy (FTIR), energy dispersive X-ray spectroscopy (EDX), X-ray photoelectron spectroscopy (XPS), Raman spectroscopy, X-ray diffraction (XRD), and transmission electron microscopy (TEM). This study presents a novel and efficient approach for synthesizing high-performance n-type thermoelectric materials for PDA-based devices by the metal doping.

2. EXPERIMENTAL SECTION

2.1. Raw Materials. DA hydrochloride powder (99%, Alfa Aesar) and tris (hydroxymethyl) aminomethane (Tris, +99.9%, Alfa Aesar) were used as received. Hydrochloric acid (HCl, AR), poly(vinyl alcohol) (PVA, ~1799, average polymerization degree is 1700 ± 50, degree of alcoholysis is 98.0−99.0%, viscosity is 25.0−31.0 mPa·s), $MnCl_2$, $ZnCl_2$, $MgCl_2{\cdot}6H_2O$, $AlCl_3{\cdot}6H_2O$, $CaCl_2$, and $FeCl_3{\cdot}6H_2O$ were produced from Chengdu Kelong Chemical Co. Ltd., China. Deionized water was produced by an ultrapure water machine with a resistance of 18.25 MΩ cm (UPH-I-10T, Ulupure Ultrapure Technology Co., Ltd.).

2.2. Preparation of PDA and Metal-PDA. DA (1 g) was added to 500 mL of tris-HCl buffer solution (containing: H_2O 176.5 mL, 0.1 M tris 250 mL, and 0.1 M HCl 73.5 mL. pH value: 8.5) to form PDA through self-polymerization. The reaction proceeded for 48 h under mechanical stirring at room temperature. The PDA powders could be obtained by filtering the solution, washing it with deionized water, and drying it overnight at 60 °C under a vacuum. For the preparation of metal-PDA, one category of inorganic salt ($ZnCl_2$, $CaCl_2$, $MnCl_2$, $FeCl_3{\cdot}6H_2O$, $MgCl_2{\cdot}6H_2O$, and $AlCl_3{\cdot}6H_2O$) was added to the Tris−HCl buffer solution while adding DA. The reaction systems were then placed at room temperature and mechanically stirred for 48 h. Similar to the synthesis of PDA, the metal-PDA powders were finally obtained by filtering the solution, washing it with deionized water, and drying it overnight under a vacuum at 60 °C.

2.3. Preparation of cPDA and Metal-cPDA. PDA, Mn-PDA, Zn-PDA, Mg-PDA, AL-PDA, Ca-PDA, and Fe-PDA powders were heat-treated in a tube furnace (GXL, 1200X, CN) under a N_2 flow (shielding gas) to obtain cPDA, Mn-cPDA, Zn-cPDA, Mg-cPDA, Al-cPDA, Ca-cPDA, and Fe-cPDA powders. In a typical run, the temperature in the furnace ramps to 800 °C at a rate of 10 °C/min and is held for 4 h. Then, it cooled to room temperature with a rate of 10 °C/min. The metal-cPDA films were produced with powders to perform the thermoelectric property test. The possible chemical structures of PDA, cPDA, and metal-cPDA are shown in Figure S1.

2.4. Characterization. The Supporting Information contains the specifics of thermoelectric characterization and thermal conductivity measurement. FTIR (Bruker Tensor 27, Germany) and Raman spectroscopy (Horiba Lab RAM HR, Japan) were recorded to analyze the structural characteristics. Scanning electron microscopy (SEM, Hitachi S-4800, Japan) with an X-ray analysis detector was employed to examine the elements composition. XPS (XSAM 800, England) with a monochromatized Al Kα X-ray source ($h\nu$ = 1486.6 eV) was used to analyze the chemical states of elements further. XRD (Philips X'Pert-MRD, Netherlands) was employed to study the crystal structure with a scanning rate of 5° min^{-1}, and TEM (Libra200, Germany) was used to study the microstructure. The carrier concentration and mobility were acquired In a Hall effect test system (HET).

3. RESULTS AND DISCUSSION

3.1. Thermoelectric Properties. As depicted in Figure 1, all metal-cPDA exhibits the reduced thermal conductivity. This is attributed to the metal ions increasing the interface or defect density within the polymers, thus, improving phonon scattering. Given the low thermal conductivity of these samples, the power factor (PF) value is employed to represent

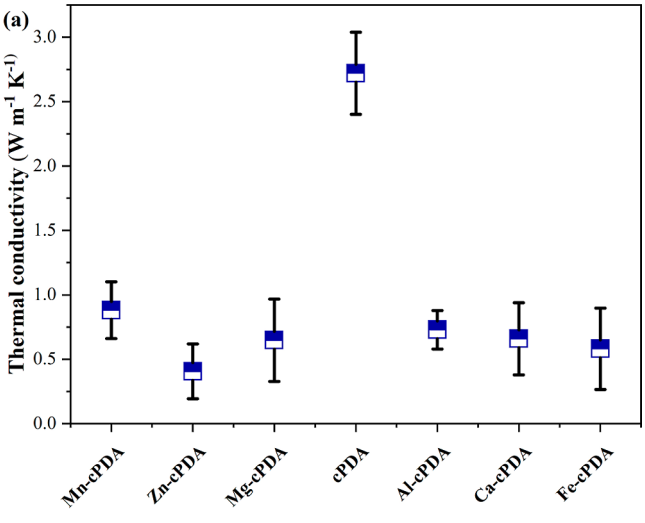

Figure 1. Thermal conductivity of cPDA and metal-cPDA at 300 K.

https://doi.org/10.1021/acsomega.4c00069
ACS Omega 2024, 9, 25812−25821

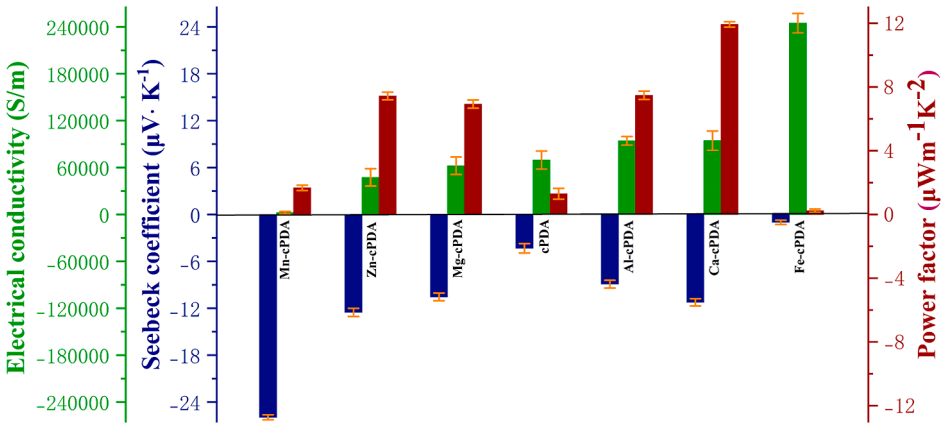

Figure 2. Electrical conductivity, Seebeck coefficient, and PF of cPDA and metal-cPDA at 300 K.

Table 1. Reported Electrical Conductivity and Seebeck Coefficient of PDA-Based Materials and Composites Containing PDA

materials [pyrolysis (T/°C)]	σ (S m^{-1})	S (μV K^{-1})	PF (μW m^{-1} K^{-2})	applied
carbonized PDA (800°C)	~1200	−5	~6 × 10^{-3}	TE[14]
Cu-PDA (800°C)	610 ± 20	9.3 ± 3.3	~5.7 × 10^{-3}	TE[18]
cPDA/SnO_2/Si (700°C)	2.6 × 10^4			lithium-ion battery[9]
Cu/PDA/GO composite (600°C)	(3.3 ± 0.5) × 10^5			Mechanical[23]
Py/PDA/CNT composite (900°C)	(4.8 ± 0.2) × 10^5			Mechanical[24]
c-CNT/PDA composite (800°C)	2.6 × 10^4	−23.5	14.4	TE[13]
c-GNS/PDA composite (800°C)	5.3 × 10^4	−11.6	7.1	TE[13]
Fe-cPDA	2.4 × 10^5	−1.0	0.2	TE (this work)
Mn-cPDA	2475	−25.9	1.7	TE (this work)
Ca-cPDA	9.4 × 10^4	−11.2	11.9	TE (this work)

their thermoelectric properties in this study. The electrical conductivity, Seebeck coefficient, and PF of all the samples at 300 K are presented in Figure 2. The PF is derived from the equation PF = $S^2\sigma$. It is observed that Zn-cPDA, Mg-cPDA, Ca-cPDA, and Fe-cPDA display higher PF values than cPDA, indicating that the incorporation of specific metal ions into cPDA enhances thermoelectric properties. All samples exhibit a negative Seebeck coefficient, which is indicative of n-type thermoelectric properties. Specifically, all metal-cPDA samples, except Fe-cPDA, exhibit higher Seebeck coefficients compared to cPDA. The peak value of the Seebeck coefficient among all the samples is achieved in Mn-cPDA, reaching −25.94 μV K^{-1}, which is more than 6 times that of cPDA. However, Mn-cPDA shows the lowest electrical conductivity of 2.47 × 10^3 S m^{-1} among these metal-cPDA samples. In contrast, Fe-cPDA displays the greatest electrical conductivity of 2.45 × 10^5 S m^{-1}, along with the lowest Seebeck coefficient of −1.00 μV K^{-1}. Ca-cPDA shows the highest PF value of 11.93 μW m^{-1} K^{-2} among these samples due to the synergistic optimization of Seebeck coefficient and electrical conductivity. Table 1 lists the reported electrical conductivity and Seebeck coefficient of PDA-based materials and composites containing PDA. For instance, the electrical conductivity of Ca-cPDA surpasses that of all of the previously reported PDA-based materials while maintaining an exceptional Seebeck coefficient. Given the superior adhesion of PDA,[13,19,20] the enhanced thermoelectric performance of PDA-based materials could serve as building a high-performance blocks and interfaces, thereby facilitating the design of innovative functional composite materials.[13,21,22]

3.2. Structural Characterization. To understand the role of metal ions in thermoelectrics properties, the detailed structural characterization was performed. Figure 3 shows the FTIR spectra of PDA, metal-PDA, cPDA, and metal-cPDA. As depicted in Figure 3a, the broad characteristic peaks of PDA, ranging from 3300−3100 cm^{-1}, are attributed to the stretching vibration of the −NH group in primary amine and −OH group in phenol structure.[9,25] Two distinct bands observed at 1440 and 1350 cm^{-1} are attributed to the stretching of C═N$^+$ or C═N$^+$−C.[26] The peaks appearing at 1282 cm^{-1} are attributed to the C−O stretching vibration inherent in the catechol structure.[27] The intensity of the characteristic peak at around 3300 cm^{-1} diminishes for all metal-PDA, a phenomenon resulting from the release of H$^+$ during the chelation process between PDA and the metal ion. It has been reported that chelation between DA and metal ions occurs in deionized water, followed by the oxidation of DA monomers upon the addition of a Tris−HCl solution. The oxidation products, 5,6-dihydroxyindole carboxylic acid (DHICA), 5,6-dihydroxyindole (DHI), and dopaquinone, also provide binding sites for metal ions.[28] The p−π conjugated system of the carbonyl group (−C═O), originating from the transition from hydroxyl group (−C−OH), effectively donates lone-pair electrons to coordinate with the empty orbitals of metal ions, thereby stabilizing the metal-PDA.[29] In detail, the peaks at 1508 cm^{-1} (corresponding to the C−N bond) show redshifts only in the spectra of Al-PDA and Fe-PDA due to the trivalent state of the metal elements. Besides, the peaks at 1440 and 1350 cm^{-1} (corresponding to C═N$^+$/C═N$^+$−C) all disappear in Fe-PDA, meaning that Fe^{3+} induces a great degree of cross-linking within PDA. As Mg (II), Ca (II), and Zn (II) are bound to the same groups (carboxylic, −COOH) under alkaline conditions, the spectra of Mg-PDA, Ca-PDA, and Zn-PDA show similar changes. After pyrolysis, as shown in Figure 3b, the strong bands at around 3200 cm^{-1} disappear in cPDA. The main

https://doi.org/10.1021/acsomega.4c00069
ACS Omega 2024, 9, 25812−25821

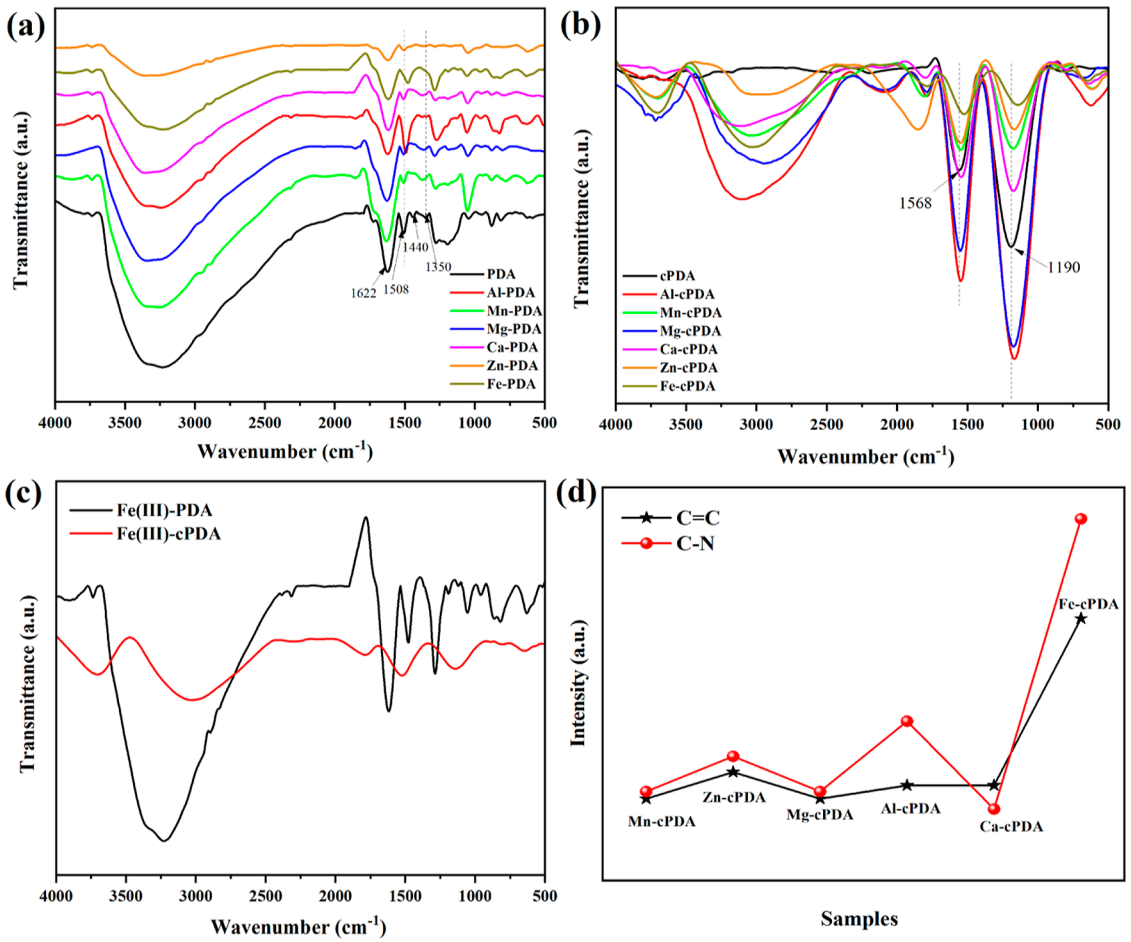

Figure 3. (a) FTIR spectra of PDA and metal-PDA. (b) FTIR spectra of cPDA and metal-cPDA. (c) FTIR spectra contrasted between Fe-PDA and Fe-cPDA. (d) Redshift of C═C and C−N in the FITR spectra for metal-cPDA.

bands at 1568 and 1190 cm^{-1} correspond to the C═C and C−N stretching vibrations,[9] respectively, coming from the nitrogen heteroaromatic sp^2 C-dominant skeleton of cPDA.[30,31] This result suggests that the amidogen and secondary amine were transformed into tertiary amines in metal-cPDA. These two characteristic peaks both redshift in metal-cPDA due to the sp^2 carbon overlap and the different active sites that coordinate with metal ions. Except for these two peaks, as shown in Figure 3c, −OH in phenol structure remains and redshifts in Fe-cPDA compared to Fe-PDA, indicating that the pyrolytic process hardly affects the chelating activity and cross-linked structure exists in metal-cPDA. In addition, the shift rate of C═C and C−N bonds, according to Figure 3b, was calculated, and the related results are shown in Figure 2d. Clearly, Fe-cPDA shows the largest shift degree compared with other metal-cPDA samples. This result further suggests that Fe^{3+} causes the greatest degree of cross-linking.[32] Furthermore, such a shift comes from $\pi-\pi$ stacking of the conjugated molecular skeleton of Fe-cPDA, which facilitates carrier transport across the molecular chains and thus increases the electrical conductivity.

The elemental results of metal-PDA and metal-cPDA by EDX are shown in Figure 4. The metal element result in Figure S2 confirms that metal ions were successfully coordinated with cPDA. Fe-cPDA has an excellent carbon yield. This phenomenon could be attributed to the liberation of various functional groups, such as carboxyl and hydroxyl, during the rearrangement of carbon atoms from a chain-like to a network-like structure. This agrees with the highest electrical conductivity, and the greatest degree of cross-linking of Fe-cPDA.

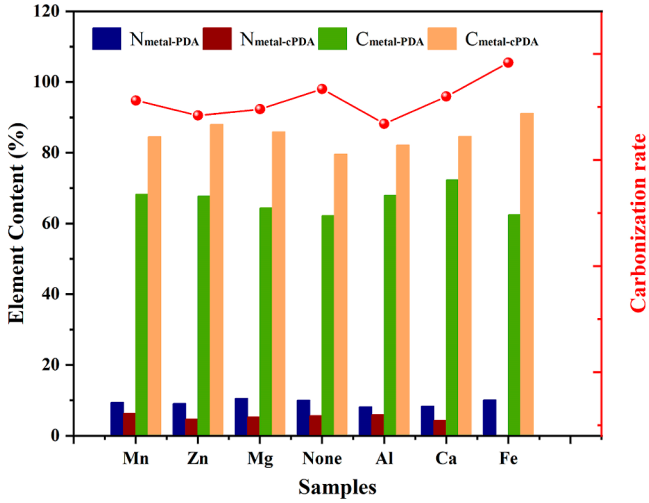

Figure 4. Elemental results of metal-PDA and metal-cPDA.

The elemental chemical states of cPDA and metal-cPDA were analyzed by using XPS. The XPS survey spectra of all samples, as depicted in Figure S3, reveal three strong signal peaks of C 1s, N 1s, and O 1s. The C 1s peak of cPDA is

https://doi.org/10.1021/acsomega.4c00069
ACS Omega 2024, 9, 25812−25821

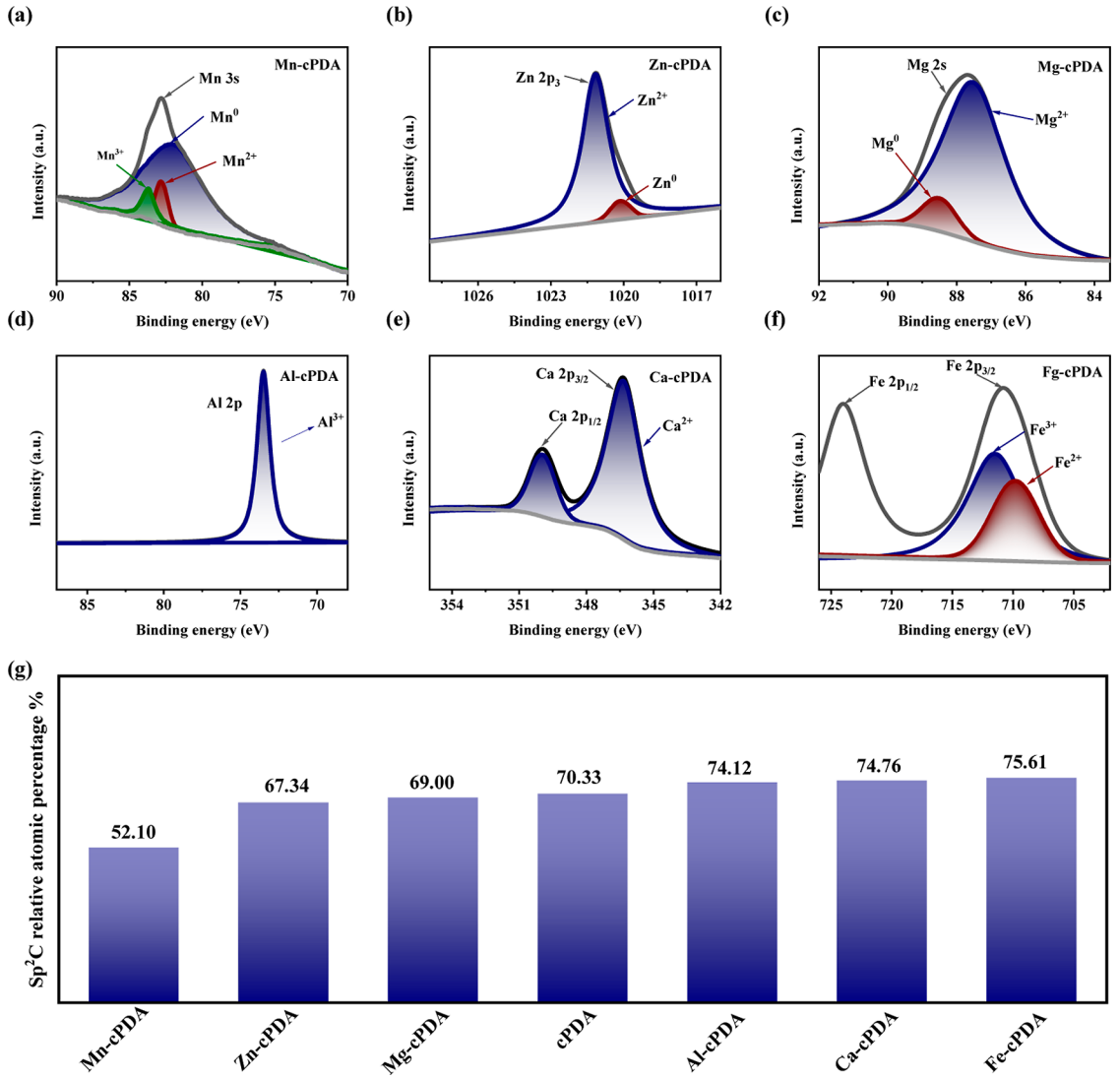

Figure 5. High-resolution XPS spectra of metal-cPDA (a–f) and sp^2 C relative atomic percentages of cPDA and metal-cPDA (g).

decomposed into three components (Figure S4a), generated by sp^2 hybridized C (284.5 eV), C–O and C=N (285.8 eV), and C–O–C and C–N (289.0 eV), respectively.[30] As shown in Figure S4b, the N 1s spectrum is decomposed into pyridine nitrogen (398.6 eV) and graphite nitrogen (401.1 eV).[33−35] Graphene-like nitrogen is converted into pyridine-like nitrogen, where graphite-N can significantly increase the limiting current density; therefore, the graphene-like nitrogen-doped structure of cPDA exhibits good electrical conductivity. After carbonization of all metal-PDA chelates at 800 °C, metal elements of different valence states formed (Figure 5a–f). Among them, the high-resolution spectra of Mn 3s of Mn-cPDA (Figure 5a) decompose into three components: about 82.1 eV of Mn metal, about 82.9 eV of Mn^{2+}, and about 83.7 eV of Mn^{3+}.[36] The Zn 2p3 (Figure 5b) characteristic peak of Zn-cPDA decomposes into two components: about 1020.1 eV of Zn metal and about 1021.1 eV of Zn^{2+}.[37] Mg 2s of Mg-cPDA (Figure 5c) have one characteristic peak that decomposes into two components: about 88.6 eV of Mg metal and about 87.6 eV of Mg^{2+}.[38] Al 2p of Al-cPDA (Figure 5d) has one characteristic peak of about 75.6 eV of Al^{3+}.[39] Ca-cPDA (Figure 5e) shows the distribution of Ca 2p as two substances: Ca $2p_{3/2}$ at ∼348.4 eV and Ca $2p_{1/2}$ at ∼352.0 eV.[40] Fe 2p of Fe-cPDA (Figure 5f) shows the Fe 2p distribution as two substances: ∼ 710 eV for Fe $2p_{3/2}$ and ∼724 eV for Fe $2p_{1/2}$, which is consistent with the previously reported spectra of Fe-containing substances doped into carbon materials. The coexistence of two antifold product peaks at ∼709.8 eV for Fe^{2+} and ∼711.5 eV for Fe^{3+} suggests that Fe may be present as Fe_3O_4 in cPDA.[41] The PDA could be considered as amorphous carbon (a-C) (a-C) containing sp^2 C and sp^3 C. The sp^3 C converts into sp^2 C as the graphitization proceeds during the high-temperature annealing.[11,30,42] The relative atomic percentage of sp^2 C to the total C species of cPDA and metal-cPDA composites is calculated in Figure 5g. The content of sp^2 C increases with the variation of chelated metal ions, corresponding to the progress of the electrical conductivity in Figure 2. This results imply that the growth of graphite-like structures is affected by the chelated metal ion in PDA. The higher degree of graphitization of metal-cPDA will induce a more ordered structure and expand the domain of $\pi-\pi$ stacking (proved by the FITR of Fe-cPDA in Figure 3d), resulting in various electrical conductivity. The evolution of graphite-like structures corresponding to various coordination metal ions in cPDA will be further confirmed by Raman spectra.

https://doi.org/10.1021/acsomega.4c00069
ACS Omega 2024, 9, 25812−25821

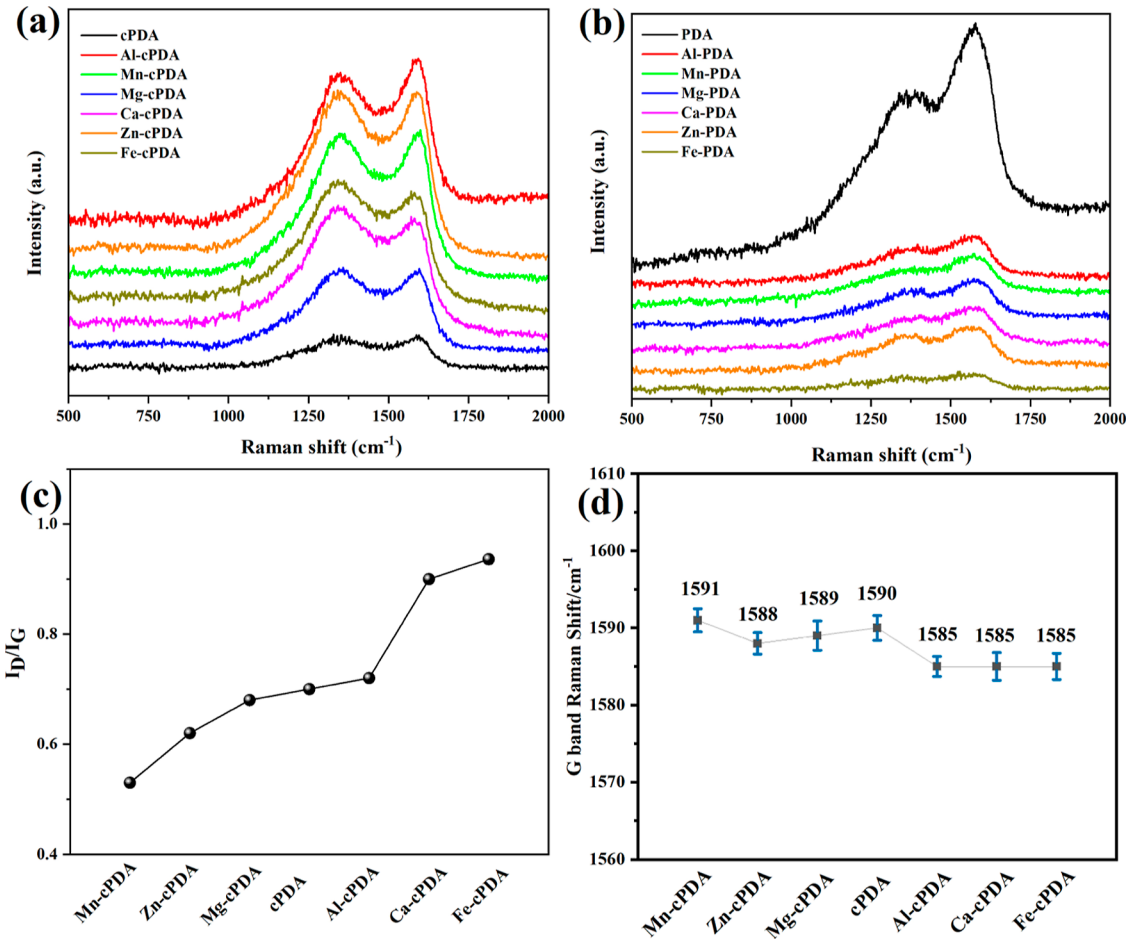

Figure 6. Raman spectra of (a) PDA, metal-PDA, and (b) cPDA, metal-cPDA. (c) I_D/I_G of cPDA and metal-cPDA. (d) G-band Raman shift of cPDA and metal-cPDA.

Raman spectra were used to further study the carbonation process of metal-cPDA, as shown in Figure 6a,b. Graphite-like characteristic peaks near the D-band (1350 cm^{-1}) and G-band (1580 cm^{-1}) are observed for all PDA and metal-PDA.[43] The intensity of the D-band and G-band exhibits stronger in metal-cPDA. This enhancement is attributed to the densification of the polymer, which results from the coordination of covalent bonds formed between the metal ions and PDA.[44] As depicted in Figure 6b, the blue shift of the G-band is observed on all the samples after the high-temperature annealing, indicating that new sp^2 tiny structure domains are produced.[14] As shown in Figure 6c, the intensity ratio of the D-band and G-band is enhanced with the variation of the doped metal ions in metal-cPDA, mirroring the progression of electrical conductivity in Figure 2. This trend aligns with the results from FITR (Figure 3d) and XPS (Figure 5g). As mentioned above, this is attributed to variations in the degree of graphitization. However, this phenomenon is not mirrored in the blue shift of the G-band in Figure 6d. According to the investigation of Ferrari and Robertson et al.,[45,46] as the perfect graphite breaks into nanocrystalline graphite (NC graphite), the I_D/I_G gradually grows, and the G band blue shifts due to the increasing of the defect. From NC graphite to a-C, I_D/I_G gradually decreases due to the reduction of the ordered sp^2 C ring and G band redshift. Thus, this tendency is reversible. In our experiment, the heat-temperature annealing facilitated the conversion from a-C to NC graphite,[14] and the increase of I_D/I_G signifies the ordering of a-C. However, the blue shift of the G-band did not follow the same trend as the increase in electrical conductivity. This discrepancy is likely due to the alteration of the sp^2 C vibrational mode, which arises from the bonds of associated impurities, including nitrogen, oxygen, and various metal ions.[47] The trend observed in the I_D/I_G ratio suggests that the conversion from a-C to NC graphite through heat-temperature annealing can be either facilitated or impeded by the variation of the doped metal ion for cPDA.

XRD patterns of the metal-cPDA depicted in Figure 7 reveal that cPDA exhibits a weak and broad diffraction peaks at 24.2° and 43.8°, corresponding to the (002) and (101) crystallographic planes of a graphite material, indicating an amorphous structure of cPDA and the presence of a short-range ordered structure in a nanographite-like state.[24] The spectra of Mn-cPDA, Zn-cPDA, Mg-cPDA, Al-cPDA, and Ca-cPDA closely resemble those of cPDA, with two prominent diffraction peaks near 24° and 43°. Notably, Fe-cPDA exhibits stronger and sharper peaks in its distinctive diffraction peaks, suggesting an enhanced degree of crystallization. This observation underscores the influence of different metal ions on the nanocrystalline properties of cPDA. Indeed, this observation aligns with the findings from FTIR, EDX, XPS, and Raman analyses. The emergence of a more ordered structure promotes the electron delocalization of $\pi-\pi$ stacking, thereby leading to an increase in electrical conductivity.[29,48] Moreover, the Fe-cPDA sample shows new characteristic diffraction peaks at 35.5° and 43.3°.

https://doi.org/10.1021/acsomega.4c00069
ACS Omega 2024, 9, 25812−25821

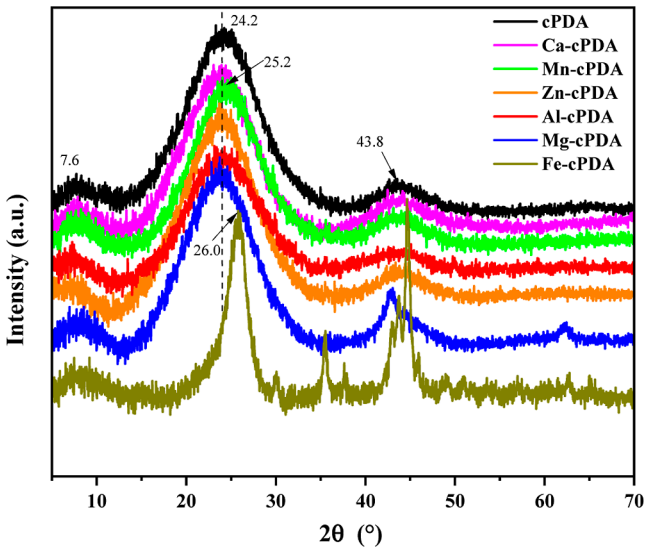

Figure 7. XRD patterns of cPDA and metal-cPDA.

By comparison with the Fe_3O_4 (PDF#261-1136) and Fe (PDF#06-0696) standard cards, the presence of weak Fe_3O_4 and Fe peak can be seen. Mg-cPDA shows new characteristic diffraction peak at 63°, which are attributed to nanometallic Mg (standard cards, PDF#35-0821). However, other metals or oxides are not shown in XRD, which may be due to their low contents.

cPDA nanoparticles (Figure S5) show uniform spherical shape and slight aggregation, and the size distribution of cPDA is about reduced to 150 nm compared to PDA (200 nm). Figure S6 shows the morphology of the metal-cPDA nanoparticles. Aggregated and irregularly shaped cPDA particles were observed in other metal-cPDA with some nanoscale features. According to XPS and XRD analysis, these black spots are nanocrystalline metals or metal oxides. It is worth noting that pore structures are observed in Fe-cPDA. Fe_3O_4 and nanocrystalline Fe in Fe-cPDA with diameters of around 30 nm in Fe-cPDA. The pore structures observed in Fe-cPDA are caused by the rearrangement of carbon atoms to form graphite nanocrystals under high-temperature annealing.

3.3. Discussion on the Thermoelectric Properties.

Comprehensive structural characterizations, especially by FTIR, XPS, and Raman spectra results, have conclusively demonstrated that the degree of graphitization or crystallinity of cPDA is relative to the specific type of metal ion. This, in turn, exerts a significant influence on the material's electrical conductivity, underscoring the pivotal role of metal ions in modulating the properties of cPDA. The carrier density and carrier mobility of cPDA and metal-cPDA, as measured by the Hall effect, are shown in Table 2. All the metal-cPDA have higher carrier mobility, which is in disagreement with the thermal conductivity results in Figure 1. This beneficial phenomenon is caused by the distinct transport mechanisms between the charge carrier and the phonon within the polymers. The metal ions create conductive paths in domain-by-domain graphite, which lowers the carrier transport barriers and enhances mobility. Meanwhile, the metal ion increases the interface or defect in the polymers, which improves phonon scattering and restrains thermal conductivity. We observe that the carrier density and carrier mobility depend on both the degree of graphitization and the metal-ion coordination. Most of metal-cPDA obtain a higher carrier density than undoped cPDA due to the coordination of metal ions, which had extremely low carrier concentration due to their low crystallinity. However, Mn-cPDA stands as an exception, displaying an extremely low carrier concentration, a characteristic likely stemming from its low crystallinity. Simultaneously, an extremely low carrier concentration reduces short-range defect scattering, thereby leading to high mobility.[49] Fe-cPDA and Ca-cPDA outperform other metal-coordinated cPDA samples in terms of both carrier density and mobility. We attribute this to the high degree of crystallinity, which boosts the delocalization of $\pi-\pi$ stacking and enables more channels to participate in the electrical transport.

Table 2. Carrier Mobility and Carrier Density of cPDA and Metal-cPDA

samples	carrier mobility (10^{-10} m^2 μV^{-1} s^{-1})	carrier density (10^{26} m^{-3})
cPDA	3.20	1.08
Mn-cPDA	10.86	0.05
Zn-cPDA	7.89	5.01
Mg-cPDA	4.51	4.11
Al-cPDA	4.44	5.40
Ca-cPDA	4.69	6.42
Fe-cPDA	8.55	10.21

In conducting polymers, the general expression of the Seebeck coefficient can be described as[50]

$$S = \frac{1}{\sigma}\frac{k_B}{q}\int \frac{E - E_f}{k_B T}\sigma_E\left(-\frac{\partial f}{\partial E}\right)dE \quad (1)$$

where k_B is the Boltzmann constant, $\sigma(E)$ is the partial electrical conductivity at energy E and generally depends on the density of state (DOS) and charge carrier velocity, and their relaxation time or hopping frequency, $\sigma = \int\sigma(E)dE$ is the total electrical conductivity, and T is temperature. As shown in eq 1, S and σ have a mutual check relationship, which is in good agreement with the thermoelectric results of Mn-cPDA and Fe-cPDA in Figure 2. The enlightened results are that the Seebeck coefficients of Zn-cPDA, Ca-cPDA, Mg-cPDA, and Al-cPDA are several times more than those of cPDA, while the electrical conductivity maintains the same level or higher. It may be owing to the drastic change in the conduction mechanism and the DOS due to the metal-ion coordination. The alteration in the conduction mechanism can be verified by the improved carrier mobility, which comes from the tuning of charge carrier velocity and their relaxation time or hopping frequency. Furthermore, metal-ion coordination could induce the increase of density-of-state effective mass, resulting in the enhancement of the Seebeck coefficient.[17,51]

4. CONCLUSIONS

In summary, we successfully synthesized a series of PDA composites with chelated metal ions, and all of the metal-PDA nanocomposites after high-temperature annealing (metal-cPDA) exhibited n-type thermoelectrical properties. At 300 K, Mn-cPDA exhibits the greatest Seebeck coefficient of -25.94 μV K^{-1} among these samples, which is almost six times higher than that of cPDA. However, it also has the lowest electrical conductivity of 2.47×10^3 S m^{-1}. On the other hand, Fe-cPDA shows the best electrical conductivity of 2.45×10^5 S m^{-1} but the worst Seebeck coefficient of -1.00 μV K^{-1}. Other samples, Zn-cPDA, Mg-cPDA, Al-cPDA, and Ca-cPDA, display higher PF values compared to cPDA. The optimal PF value of

https://doi.org/10.1021/acsomega.4c00069
ACS Omega 2024, 9, 25812−25821

11.93 μW m^{-1} K^{-2} is in Ca-cPDA, with enhanced electrical conductivity of 9.5 × 10^4 S m^{-1} and a Seebeck coefficient of −11.24 μV K^{-1}.

Further structural characterization reveals that Fe-cPDA has the most extensive degree of cross-linking by FTIR, the excellent carbon yield by EDX, and the highest degree of crystallinity by XRD, corresponding to the highest electrical conductivity. Moreover, the redshift of C=C and C−N in FITR spectra, the content of Sp^2 C in XPS spectra, and the ratio of I_D/I_G in Raman spectra, with various metal ion chelation, all exhibit a consistent trend as the electrical conductivity. These results indicate that the growth of graphite-like structures for metal-PDA under high-temperature annealing carbonization can be modulated by the various chelated metals. Compared to the metal-undoped cPDA, the chelation with Fe^{2+} and Ca^{2+} will promote the conversion from a-C to nanocrystalline graphite, and the chelation with Al^{3+}, Mg^{2+}, and Zn^{2+} has no obvious influence, but the chelation with Mn^{2+} will hinder it. The higher degree of graphitization induces a more ordered structure and expands the domain of $\pi-\pi$ stacking, boosting the electrical conductivity. We observe that the carrier density and carrier mobility depend on both the degree of graphitization and the metal-ion coordination, which work together on electrical conductivity and Seebeck coefficient. The degree of graphitization of Mn-cPDA is extremely low, resulting in extremely low carrier concentrations. Most of the metal-cPDA samples exhibit higher carrier density and carrier mobility due to the metal-coordination.

■ ASSOCIATED CONTENT

Supporting Information

The Supporting Information is available free of charge at https://pubs.acs.org/doi/10.1021/acsomega.4c00069.

Additional information on the measurement details of electrical conductivity, Seebeck coefficient, and thermal conductivity; possible chemical structure of PDA, cPDA, and metal-cPDA; metal elemental result of metal-cPDA, and XPS survey spectra of Mn-cPDA, Zn-cPDA, Mg-cPDA, Al-cPDA, Ca-cPDA, and Fe-cPDA spheres; C 1s and N 1s high-resolution XPS spectrum of cPDA; and SEM images of PDA and TEM images of cPDA and metal-cPDA (PDF)

■ AUTHOR INFORMATION

Corresponding Authors

Zhijun Wang − *Institute for Advanced Study, Chengdu University, Chengdu 610106, P. R. China*; Email: wangzhijun@cdu.edu.cn

Yihan Wang − *Key Laboratory of Radiation Physics and Technology of the Ministry of Education, Institute of Nuclear Science and Technology, Sichuan University, Chengdu 610064, P. R. China*; orcid.org/0000-0003-3325-2231; Email: yhwang027@scu.edu.cn

Authors

Qi Zhu − *Key Laboratory of Radiation Physics and Technology of the Ministry of Education, Institute of Nuclear Science and Technology, Sichuan University, Chengdu 610064, P. R. China; Institute for Advanced Study, Chengdu University, Chengdu 610106, P. R. China*

Hongwen Cao − *Key Laboratory of Radiation Physics and Technology of the Ministry of Education, Institute of Nuclear Science and Technology, Sichuan University, Chengdu 610064, P. R. China*

Ziheng Xu − *Key Laboratory of Radiation Physics and Technology of the Ministry of Education, Institute of Nuclear Science and Technology, Sichuan University, Chengdu 610064, P. R. China*

Rui Zhong − *Key Laboratory of Radiation Physics and Technology of the Ministry of Education, Institute of Nuclear Science and Technology, Sichuan University, Chengdu 610064, P. R. China*

Bo Jiang − *College of Chemistry, Sichuan University, Chengdu 610064, P. R. China*

Qinjian Yin − *College of Chemistry, Sichuan University, Chengdu 610064, P. R. China*

Kun Zhang − *Key Laboratory of Radiation Physics and Technology of the Ministry of Education, Institute of Nuclear Science and Technology, Sichuan University, Chengdu 610064, P. R. China*

Complete contact information is available at: https://pubs.acs.org/10.1021/acsomega.4c00069

Notes

The authors declare no competing financial interest.

■ ACKNOWLEDGMENTS

This work has been supported by the Fundamental Research Funds for the Central Universities (no. 2022SCU12124) and the National Natural Science Foundation of China (NSFC) (no. 51973127) and (no. 52203232). We are thankful to the Experimental Testing Center College of Chemistry, Sichuan University, for their help in sample analysis.

■ REFERENCES

(1) Lv, H.; Liang, L.; Zhang, Y.; Deng, L.; Chen, Z.; Liu, Z.; Wang, H.; Chen, G. A Flexible Spring-Shaped Architecture with Optimized Thermal Design for Wearable Thermoelectric Energy Harvesting. *Nano Energy* **2021**, *88*, 106260.

(2) Angrist, S. W. *Direct Energy Conversion*; U.S. Department of Energy: United States, 1976; .

(3) Zhao, L.-D.; He, J.; Berardan, D.; Lin, Y.; Li, J.-F.; Nan, C.-W.; Dragoe, N. BiCuSeO Oxyselenides: New Promising Thermoelectric Materials. *Energy Environ. Sci.* **2014**, *7* (9), 2900−2924.

(4) Aswal, D. K.; Basu, R.; Singh, A. Key Issues in Development of Thermoelectric Power Generators: High Figure-of-Merit Materials and Their Highly Conducting Interfaces with Metallic Interconnects. *Energy Convers. Manage.* **2016**, *114*, 50−67.

(5) Bounioux, C.; Díaz-Chao, P.; Campoy-Quiles, M.; Martín-González, M. S.; Goñi, A. R.; Yerushalmi-Rozen, R.; Müller, C. Thermoelectric Composites of Poly(3-Hexylthiophene) and Carbon Nanotubes with a Large Power Factor. *Energy Environ. Sci.* **2013**, *6* (3), 918.

(6) Bubnova, O.; Khan, Z. U.; Malti, A.; Braun, S.; Fahlman, M.; Berggren, M.; Crispin, X. Optimization of the Thermoelectric Figure of Merit in the Conducting Polymer Poly(3,4-Ethylenedioxythiophene). *Nat. Mater.* **2011**, *10* (6), 429−433.

(7) Xu, S.; Shi, X.-L.; Dargusch, M.; Di, C.; Zou, J.; Chen, Z.-G. Conducting Polymer-Based Flexible Thermoelectric Materials and Devices: From Mechanisms to Applications. *Prog. Mater. Sci.* **2021**, *121*, 100840.

(8) Liu, Y.; Ai, K.; Lu, L. Polydopamine and Its Derivative Materials: Synthesis and Promising Applications in Energy, Environmental, and Biomedical Fields. *Chem. Rev.* **2014**, *114* (9), 5057−5115.

(9) Kong, J.; Yee, W. A.; Yang, L.; Wei, Y.; Phua, S. L.; Ong, H. G.; Ang, J. M.; Li, X.; Lu, X. Highly Electrically Conductive Layered Carbon Derived from Polydopamine and Its Functions in SnO2-

Based Lithium Ion Battery Anodes. *Chem. Commun.* **2012**, *48* (83), 10316.
(10) Yuan, H.; Wang, Y.; Li, T.; Ma, P.; Zhang, S.; Du, M.; Chen, M.; Dong, W.; Ming, W. Highly Thermal Conductive and Electrically Insulating Polymer Composites Based on Polydopamine-Coated Copper Nanowire. *Compos. Sci. Technol.* **2018**, *164*, 153−159.
(11) Yu, X.; Fan, H.; Liu, Y.; Shi, Z.; Jin, Z. Characterization of Carbonized Polydopamine Nanoparticles Suggests Ordered Supramolecular Structure of Polydopamine. *Langmuir* **2014**, *30* (19), 5497−5505.
(12) Li, R.; Parvez, K.; Hinkel, F.; Feng, X.; Müllen, K. Bioinspired Wafer-Scale Production of Highly Stretchable Carbon Films for Transparent Conductive Electrodes. *Angew. Chem., Int. Ed.* **2013**, *52* (21), 5535−5538.
(13) Wang, Y.; Wu, S.; Yin, Q.; Du, K.; Yin, Q.; Jiang, B.; Mo, S. Novel Hybrid P- and n-Type Organic Thermoelectric Materials Based on Mussel-Inspired Polydopamine. *ACS Appl. Mater. Interfaces* **2021**, *13* (20), 23970−23982.
(14) Li, H.; Aulin, Y. V.; Frazer, L.; Borguet, E.; Kakodkar, R.; Feser, J.; Chen, Y.; An, K.; Dikin, D. A.; Ren, F. Structure Evolution and Thermoelectric Properties of Carbonized Polydopamine Thin Films. *ACS Appl. Mater. Interfaces* **2017**, *9* (8), 6655−6660.
(15) Yong, X.; Shi, W.; Wu, G.; Goh, S. S.; Bai, S.; Xu, J.-W.; Wang, J.-S.; Yang, S.-W. Tuning the Thermoelectric Performance of π-d Conjugated Nickel Coordination Polymers through Metal-Ligand Frontier Molecular Orbital Alignment. *J. Mater. Chem. A* **2018**, *6* (40), 19757−19766.
(16) Sun, Y.; Sheng, P.; Di, C.; Jiao, F.; Xu, W.; Qiu, D.; Zhu, D. Organic Thermoelectric Materials and Devices Based on P- and n-Type Poly(Metal 1,1,2,2-Ethenetetrathiolate)s. *Adv. Mater.* **2012**, *24* (7), 932−937.
(17) Sun, Y.; Qiu, L.; Tang, L.; Geng, H.; Wang, H.; Zhang, F.; Huang, D.; Xu, W.; Yue, P.; Guan, Y.; Jiao, F.; Sun, Y.; Tang, D.; Di, C.; Yi, Y.; Zhu, D. Flexible N-Type High-Performance Thermoelectric Thin Films of Poly(Nickel-Ethylenetetrathiolate) Prepared by an Electrochemical Method. *Adv. Mater.* **2016**, *28* (17), 3351−3358.
(18) Li, H.; Marshall, T.; Aulin, Y. V.; Thenuwara, A. C.; Zhao, Y.; Borguet, E.; Strongin, D. R.; Ren, F. Structural Evolution and Electrical Properties of Metal Ion-Containing Polydopamine. *J. Mater. Sci.* **2019**, *54* (8), 6393−6400.
(19) Nam, H. J.; Kim, B.; Ko, M. J.; Jin, M.; Kim, J. M.; Jung, D. A New Mussel-Inspired Polydopamine Sensitizer for Dye-Sensitized Solar Cells: Controlled Synthesis and Charge Transfer. *Chem.—Eur. J.* **2012**, *18* (44), 14000−14007.
(20) Lee, H.; Dellatore, S. M.; Miller, W. M.; Messersmith, P. B. Mussel-Inspired Surface Chemistry for Multifunctional Coatings. *Science* **2007**, *318* (5849), 426−430.
(21) Qi, X.; Huang, Y.; You, S.; Xiang, Y.; Cai, E.; Mao, R.; Pan, W.; Tong, X.; Dong, W.; Ye, F.; Shen, J. Engineering Robust Ag-Decorated Polydopamine Nano-Photothermal Platforms to Combat Bacterial Infection and Prompt Wound Healing. *Adv. Sci.* **2022**, *9* (11), 2106015.
(22) Liu, L.; Zhang, H.; Peng, L.; Wang, D.; Zhang, Y.; Yan, B.; Xie, J.; Xing, S.; Peng, F.; Liu, X. A Copper-Metal Organic Framework Enhances the Photothermal and Chemodynamic Properties of Polydopamine for Melanoma Therapy. *Acta Biomater.* **2023**, *158*, 660−672.
(23) Jia, Z.; Li, H.; Zhao, Y.; Frazer, L.; Qian, B.; Borguet, E.; Ren, F.; Dikin, D. A. Electrical and Mechanical Properties of Poly-(Dopamine)-Modified Copper/Reduced Graphene Oxide Composites. *J. Mater. Sci.* **2017**, *52* (19), 11620−11629.
(24) Ryu, S.; Chou, J. B.; Lee, K.; Lee, D.; Hong, S. H.; Zhao, R.; Lee, H.; Kim, S. Direct Insulation-to-Conduction Transformation of Adhesive Catecholamine for Simultaneous Increases of Electrical Conductivity and Mechanical Strength of CNT Fibers. *Adv. Mater.* **2015**, *27* (21), 3250−3255.
(25) Luo, J.; Jiang, S.; Liu, X. Efficient One-Pot Synthesis of Mussel-Inspired Molecularly Imprinted Polymer Coated Graphene for Protein-Specific Recognition and Fast Separation. *J. Phys. Chem. C* **2013**, *117* (36), 18448−18456.
(26) Yu, K.; Wang, J.; Wang, X.; Liang, J.; Liang, C. Sustainable Application of Biomass By-Products: Corn Straw-Derived Porous Carbon Nanospheres Using as Anode Materials for Lithium Ion Batteries. *Mater. Chem. Phys.* **2020**, *243*, 122644.
(27) Ho, C.-C.; Ding, S.-J. The pH-Controlled Nanoparticles Size of Polydopamine for Anti-Cancer Drug Delivery. *J. Mater. Sci.: Mater. Med.* **2013**, *24* (10), 2381−2390.
(28) Ryu, J. H.; Messersmith, P. B.; Lee, H. Polydopamine Surface Chemistry: A Decade of Discovery. *ACS Appl. Mater. Interfaces* **2018**, *10* (9), 7523−7540.
(29) Hong, G.; Shen, L.; Wang, M.; Yang, Y.; Wang, X.; Zhu, M.; Hsiao, B. S. Nanofibrous Polydopamine Complex Membranes for Adsorption of Lanthanum (III) Ions. *Chem. Eng. J.* **2014**, *244*, 307−316.
(30) Ai, K.; Liu, Y.; Ruan, C.; Lu, L.; Lu, G. M. Sp ^{2} C-Dominant N-Doped Carbon Sub-Micrometer Spheres with a Tunable Size: A Versatile Platform for Highly Efficient Oxygen-Reduction Catalysts. *Adv. Mater.* **2013**, *25* (7), 998−1003.
(31) Lei, C.; Han, F.; Li, D.; Li, W.-C.; Sun, Q.; Zhang, X.-Q.; Lu, A.-H. Dopamine as the Coating Agent and Carbon Precursor for the Fabrication of N-Doped Carbon Coated Fe3O4 Composites as Superior Lithium Ion Anodes. *Nanoscale* **2013**, *5* (3), 1168.
(32) Monahan, J.; Wilker, J. J. Specificity of Metal Ion Cross-Linking in Marine Mussel Adhesives. *Chem. Commun.* **2003**, No. 14, 1672.
(33) Chen, S.; Bi, J.; Zhao, Y.; Yang, L.; Zhang, C.; Ma, Y.; Wu, Q.; Wang, X.; Hu, Z. Nitrogen-Doped Carbon Nanocages as Efficient Metal-Free Electrocatalysts for Oxygen Reduction Reaction. *Adv. Mater.* **2012**, *24* (41), 5593−5597.
(34) Wu, G.; Zelenay, P. Nanostructured Nonprecious Metal Catalysts for Oxygen Reduction Reaction. *Acc. Chem. Res.* **2013**, *46* (8), 1878−1889.
(35) Sharifi, T.; Hu, G.; Jia, X.; Wågberg, T. Formation of Active Sites for Oxygen Reduction Reactions by Transformation of Nitrogen Functionalities in Nitrogen-Doped Carbon Nanotubes. *ACS Nano* **2012**, *6* (10), 8904−8912.
(36) Miao, Z.-H.; Wang, H.; Yang, H.; Li, Z.-L.; Zhen, L.; Xu, C.-Y. Intrinsically Mn $^{2+}$ -Chelated Polydopamine Nanoparticles for Simultaneous Magnetic Resonance Imaging and Photothermal Ablation of Cancer Cells. *ACS Appl. Mater. Interfaces* **2015**, *7* (31), 16946−16952.
(37) Strohmeier, B. R.; Leyden, D. E.; Scottfield, R.; Hercules', D. M. Surface Spectroscopic Characterization of Cu/Al_20_3 Catalysts. *J. Catal.* **1985**, *94*, 514.
(38) Peng, X. D.; Barteau, M. A. Characterization of Oxide Layers on Mg(OOO1) and comparison of H,O adsorption on surface and bulk oxides. *Surf. Sci.* **1990**, *233*, 283.
(39) Kim, Y.-C.; Park, H.-H.; Chun, J. S.; Lee, W.-J. Compositional and Structural Analysis of Aluminum Oxide Films Prepared by Plasma-Enhanced Chemical Vapor Deposition. *Thin Solid Films* **1994**, *237* (1−2), 57−65.
(40) Sosulnikov, M. I.; Teterin, Yu. A. X-Ray Photoelectron Studies of Ca, Sr and Ba and Their Oxides and Carbonates. *J. Electron Spectrosc. Relat. Phenom.* **1992**, *59* (2), 111−126.
(41) Hawn, D. D.; DeKoven, B. M. Deconvolution as a Correction for Photoelectron Inelastic Energy Losses in the Core Level XPS Spectra of Iron Oxides. *Surf. Interface Anal.* **1987**, *10* (2−3), 63−74.
(42) Kong, J.; Seyed Shahabadi, S. I.; Lu, X. Integration of Inorganic Nanostructures with Polydopamine-Derived Carbon: Tunable Morphologies and Versatile Applications. *Nanoscale* **2016**, *8* (4), 1770−1788.
(43) Ferrari, A. C. Raman Spectroscopy of Graphene and Graphite: Disorder, Electron-Phonon Coupling, Doping and Nonadiabatic Effects. *Solid State Commun.* **2007**, *143* (1−2), 47−57.
(44) Alotaibi, F.; Tung, T. T.; Nine, M. J.; Kabiri, S.; Moussa, M.; Tran, D. N. H.; Losic, D. Scanning Atmospheric Plasma for Ultrafast Reduction of Graphene Oxide and Fabrication of Highly Conductive Graphene Films and Patterns. *Carbon* **2018**, *127*, 113−121.

https://doi.org/10.1021/acsomega.4c00069
ACS Omega 2024, 9, 25812−25821

(45) Ferrari, A. C.; Robertson, J. Interpretation of Raman Spectra of Disordered and Amorphous Carbon. *Phys. Rev. B* **2000**, *61* (20), 14095−14107.
(46) Ferrari, A. C.; Robertson, J. Raman Spectroscopy of Amorphous, Nanostructured, Diamond-like Carbon, and Nanodiamond. *Philos. Trans. R. Soc. London, Ser. A* **2004**, *362* (1824), 2477−2512.
(47) Li, Z.; Biris, A. S.; Dervishi, E.; Saini, V.; Xu, Y.; Biris, A. R.; Lupu, D. Influence of Impurities on the X-Ray Photoelectron Spectroscopy and Raman Spectra of Single-Wall Carbon Nanotubes. *J. Chem. Phys.* **2007**, *127* (15), 154713.
(48) Heffner, G. W.; Dahman, S. J.; Pearson, D. S.; Gettinger, C. L. The Effect of Molecular Weight and Crystallinity on the Conductivity of a Conducting Polymer. *Polymer* **1993**, *34* (15), 3155−3159.
(49) Gosling, J. H.; Makarovsky, O.; Wang, F.; Cottam, N. D.; Greenaway, M. T.; Patanè, A.; Wildman, R. D.; Tuck, C. J.; Turyanska, L.; Fromhold, T. M. Universal Mobility Characteristics of Graphene Originating from Charge Scattering by Ionised Impurities. *Commun. Phys.* **2021**, *4* (1), 30.
(50) Kang, S. D.; Snyder, G. J. Charge-Transport Model for Conducting Polymers. *Nat. Mater.* **2017**, *16* (2), 252−257.
(51) Shi, W.; Wu, G.; Yong, X.; Deng, T.; Wang, J.-S.; Zheng, J.-C.; Xu, J.; Sullivan, M. B.; Yang, S.-W. Orbital-Engineering-Based Screening of π-Conjugated d ^{8} Transition-Metal Coordination Polymers for High-Performance n-Type Thermoelectric Applications. *ACS Appl. Mater. Interfaces* **2018**, *10* (41), 35306−35315.

https://doi.org/10.1021/acsomega.4c00069
ACS Omega 2024, 9, 25812−25821